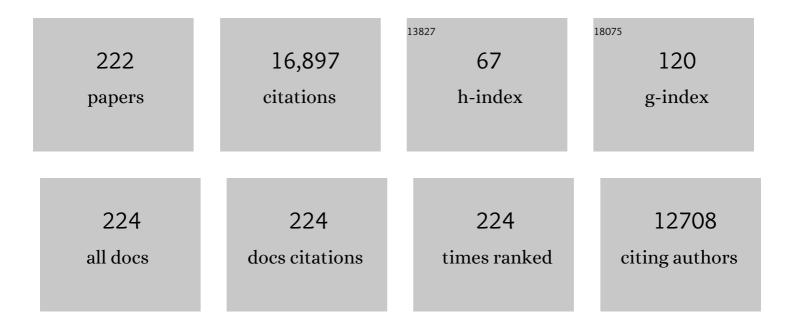
List of Publications by Year in descending order

Source: https://exaly.com/author-pdf/3200711/publications.pdf Version: 2024-02-01



Ζηένητα 2011

#	Article	IF	CITATIONS
1	Spatial-temporal variation of satellite-based gross primary production estimation in wheat-maize rotation area during 2000–2015. Geocarto International, 2022, 37, 2506-2523.	1.7	3
2	Large spatial variation and stagnation of cropland gross primary production increases the challenges of sustainable grain production and food security in China. Science of the Total Environment, 2022, 811, 151408.	3.9	17
3	Quantifying latitudinal variation in land surface phenology of Spartina alterniflora saltmarshes across coastal wetlands in China by Landsat 7/8 and Sentinel-2 images. Remote Sensing of Environment, 2022, 269, 112810.	4.6	30
4	Meteorological Influences on Spatiotemporal Variation of PM2.5 Concentrations in Atmospheric Pollution Transmission Channel Cities of the Beijing–Tianjin–Hebei Region, China. International Journal of Environmental Research and Public Health, 2022, 19, 1607.	1.2	10
5	A large but transient carbon sink from urbanization and rural depopulation in China. Nature Sustainability, 2022, 5, 321-328.	11.5	130
6	Evolution of light use efficiency models: Improvement, uncertainties, and implications. Agricultural and Forest Meteorology, 2022, 317, 108905.	1.9	62
7	Rapid surface water expansion due to increasing artificial reservoirs and aquaculture ponds in North China Plain. Journal of Hydrology, 2022, 608, 127637.	2.3	21
8	Annual 30-m big Lake Maps of the Tibetan Plateau in 1991–2018. Scientific Data, 2022, 9, 164.	2.4	14
9	Temporal Dynamics of Bacterial Communities along a Gradient of Disturbance in a U.S. Southern Plains Agroecosystem. MBio, 2022, 13, e0382921.	1.8	4
10	Large loss and rapid recovery of vegetation cover and aboveground biomass over forest areas in Australia during 2019–2020. Remote Sensing of Environment, 2022, 278, 113087.	4.6	26
11	Satellite-Based Surface Water Storage Estimation: Its history, current status, and future prospects. IEEE Geoscience and Remote Sensing Magazine, 2022, 10, 10-31.	4.9	3
12	Contributions of sea–land breeze and local climate zones to daytime and nighttime heat island intensity. Npj Urban Sustainability, 2022, 2, .	3.7	34
13	Urban ventilation corridors and spatiotemporal divergence patterns of urban heat island intensity: a local climate zone perspective. Environmental Science and Pollution Research, 2022, 29, 74394-74406.	2.7	24
14	Assimilating remote sensing-based VPM GPP into the WOFOST model for improving regional winter wheat yield estimation. European Journal of Agronomy, 2022, 139, 126556.	1.9	17
15	Dormant Season Vegetation Phenology and Eddy Fluxes in Native Tallgrass Prairies of the U.S. Southern Plains. Remote Sensing, 2022, 14, 2620.	1.8	3
16	Small anomalies in dry-season greenness and chlorophyll fluorescence for Amazon moist tropical forests during El Niño and La Niña. Remote Sensing of Environment, 2021, 253, 112196.	4.6	21
17	Spatial-temporal dynamics of maize and soybean planted area, harvested area, gross primary production, and grain production in the Contiguous United States during 2008-2018. Agricultural and Forest Meteorology, 2021, 297, 108240.	1.9	12
18	Assessing variability of optimum air temperature for photosynthesis across site-years, sites and biomes and their effects on photosynthesis estimation. Agricultural and Forest Meteorology, 2021, 298-299, 108277.	1.9	8

#	Article	IF	CITATIONS
19	Forest Changes by Precipitation Zones in Northern China after the Three-North Shelterbelt Forest Program in China. Remote Sensing, 2021, 13, 543.	1.8	17
20	Reply to: "Correlation between paddy rice growth and satellite-observed methane column abundance does not imply causation― Nature Communications, 2021, 12, 1189.	5.8	1
21	The 10-m crop type maps in Northeast China during 2017–2019. Scientific Data, 2021, 8, 41.	2.4	141
22	From Standard Weather Stations to Virtual Micro-Meteorological Towers in Ungauged Sites: Modeling Tool for Surface Energy Fluxes, Evapotranspiration, Soil Temperature, and Soil Moisture Estimations. Remote Sensing, 2021, 13, 1271.	1.8	2
23	Spatiotemporal Changes of Winter Wheat Planted and Harvested Areas, Photosynthesis and Grain Production in the Contiguous United States from 2008–2018. Remote Sensing, 2021, 13, 1735.	1.8	6
24	Carbon loss from forest degradation exceeds that from deforestation in the Brazilian Amazon. Nature Climate Change, 2021, 11, 442-448.	8.1	166
25	Characterizing Wetland Inundation and Vegetation Dynamics in the Arctic Coastal Plain Using Recent Satellite Data and Field Photos. Remote Sensing, 2021, 13, 1492.	1.8	6
26	Globalâ€Scale Consistency of Spaceborne Vegetation Indices, Chlorophyll Fluorescence, and Photosynthesis. Journal of Geophysical Research G: Biogeosciences, 2021, 126, e2020JG006136.	1.3	21
27	Temporal Changes of Virus-Like Particle Abundance and Metagenomic Comparison of Viral Communities in Cropland and Prairie Soils. MSphere, 2021, 6, e0116020.	1.3	12
28	Mapping Panax Notoginseng Plantations by Using an Integrated Pixel- and Object-Based (IPOB) Approach and ZY-3 Imagery. Remote Sensing, 2021, 13, 2184.	1.8	2
29	Annual Maps of Forests in Australia from Analyses of Microwave and Optical Images with FAO Forest Definition. Journal of Remote Sensing, 2021, 2021, .	3.2	3
30	Impacts of juniper woody plant encroachment into grasslands on local climate. Agricultural and Forest Meteorology, 2021, 307, 108508.	1.9	21
31	Spatially explicit changes in forest biomass carbon of China over the past 4 decades: Coupling long-term inventory and remote sensing data. Journal of Cleaner Production, 2021, 316, 128274.	4.6	9
32	Contribution of urban ventilation to the thermal environment and urban energy demand: Different climate background perspectives. Science of the Total Environment, 2021, 795, 148791.	3.9	105
33	Spatial extrapolation of topographic models for mapping soil organic carbon using local samples. Geoderma, 2021, 404, 115290.	2.3	8
34	Estimation of the relative contributions of forest areal expansion and growth to China's forest stand biomass carbon sequestration from 1977 to 2018. Journal of Environmental Management, 2021, 300, 113757.	3.8	16
35	Mapping forest in the southern Great Plains with ALOS-2 PALSAR-2 and Landsat 7/8 data. International Journal of Applied Earth Observation and Geoinformation, 2021, 104, 102578.	1.4	3
36	Rebound in China's coastal wetlands following conservation and restoration. Nature Sustainability, 2021, 4, 1076-1083.	11.5	103

#	Article	IF	CITATIONS
37	Improving a Biogeochemical Model to Simulate Microbialâ€mediated Carbon Dynamics in Agricultural ecosystems. Journal of Advances in Modeling Earth Systems, 2021, 13, e2021MS002752.	1.3	1
38	Global distribution, trends, and drivers of flash drought occurrence. Nature Communications, 2021, 12, 6330.	5.8	130
39	Climate Change and Livestock Management Drove Extensive Vegetation Recovery in the Qinghai-Tibet Plateau. Remote Sensing, 2021, 13, 4808.	1.8	3
40	Patterns of soil nitrogen mineralization under a landâ€use change from desert to farmland. European Journal of Soil Science, 2020, 71, 60-68.	1.8	10
41	Tracking annual changes of coastal tidal flats in China during 1986–2016 through analyses of Landsat images with Google Earth Engine. Remote Sensing of Environment, 2020, 238, 110987.	4.6	146
42	Tracking the phenology and expansion of Spartina alterniflora coastal wetland by time series MODIS and Landsat images. Multimedia Tools and Applications, 2020, 79, 5175-5195.	2.6	11
43	Enhanced spring phenological temperature sensitivity explains the extension of carbon uptake period in temperate forest protected areas. Forest Ecology and Management, 2020, 455, 117679.	1.4	9
44	Assessing the impact of climate changes on the potential yields of maize and paddy rice in Northeast China by 2050. Theoretical and Applied Climatology, 2020, 140, 167-182.	1.3	13
45	Performance of four state-of-the-art GPP products (VPM, MOD17, BESS and PML) for grasslands in drought years. Ecological Informatics, 2020, 56, 101052.	2.3	42
46	Forest management in southern China generates short term extensive carbon sequestration. Nature Communications, 2020, 11, 129.	5.8	259
47	Large increases of paddy rice area, gross primary production, and grain production in Northeast China during 2000–2017. Science of the Total Environment, 2020, 711, 135183.	3.9	104
48	Understanding the Land Surface Phenology and Gross Primary Production of Sugarcane Plantations by Eddy Flux Measurements, MODIS Images, and Data-Driven Models. Remote Sensing, 2020, 12, 2186.	1.8	13
49	Spatiotemporal patterns of vegetation phenology along the urban–rural gradient in Coastal Dalian, China. Urban Forestry and Urban Greening, 2020, 54, 126784.	2.3	46
50	High-Precision Stand Age Data Facilitate the Estimation of Rubber Plantation Biomass: A Case Study of Hainan Island, China. Remote Sensing, 2020, 12, 3853.	1.8	10
51	Differential responses of native and managed prairie pastures to environmental variability and management practices. Agricultural and Forest Meteorology, 2020, 294, 108137.	1.9	4
52	Mapping sugarcane plantation dynamics in Guangxi, China, by time series Sentinel-1, Sentinel-2 and Landsat images. Remote Sensing of Environment, 2020, 247, 111951.	4.6	105
53	Quantifying expansion and removal of Spartina alterniflora on Chongming island, China, using time series Landsat images during 1995–2018. Remote Sensing of Environment, 2020, 247, 111916.	4.6	63
54	Identifying floods and flood-affected paddy rice fields in Bangladesh based on Sentinel-1 imagery and Google Earth Engine. ISPRS Journal of Photogrammetry and Remote Sensing, 2020, 166, 278-293.	4.9	89

#	Article	IF	CITATIONS
55	Gainers and losers of surface and terrestrial water resources in China during 1989–2016. Nature Communications, 2020, 11, 3471.	5.8	81
56	Estimating site-specific optimum air temperature and assessing its effect on the photosynthesis of grasslands in mid- to high-latitudes. Environmental Research Letters, 2020, 15, 034064.	2.2	16
57	Grassland Wildfires in the Southern Great Plains: Monitoring Ecological Impacts and Recovery. Remote Sensing, 2020, 12, 619.	1.8	9
58	Mapping Forested Wetland Inundation in the Delmarva Peninsula, USA Using Deep Convolutional Neural Networks. Remote Sensing, 2020, 12, 644.	1.8	35
59	Fingerprint of rice paddies in spatial–temporal dynamics of atmospheric methane concentration in monsoon Asia. Nature Communications, 2020, 11, 554.	5.8	56
60	Synergistic China–US Ecological Research is Essential for Global Emerging Infectious Disease Preparedness. EcoHealth, 2020, 17, 160-173.	0.9	30
61	Mapping coastal wetlands of China using time series Landsat images in 2018 and Google Earth Engine. ISPRS Journal of Photogrammetry and Remote Sensing, 2020, 163, 312-326.	4.9	138
62	Impact of spring phenology variation on GPP and its lag feedback for winter wheat over the North China Plain. Science of the Total Environment, 2020, 725, 138342.	3.9	10
63	Dynamical Downscaling of CO ₂ in 2016 Over the Contiguous United States Using WRFâ€VPRM, a Weatherâ€Biosphereâ€Onlineâ€Coupled Model. Journal of Advances in Modeling Earth Systems, 2020, 12, e2019MS001875.	1.3	21
64	Estimating Forest Stock Volume in Hunan Province, China, by Integrating In Situ Plot Data, Sentinel-2 Images, and Linear and Machine Learning Regression Models. Remote Sensing, 2020, 12, 186.	1.8	44
65	The 2012 Flash Drought Threatened US Midwest Agroecosystems. Chinese Geographical Science, 2019, 29, 768-783.	1.2	48
66	Satellite-observed pantropical carbon dynamics. Nature Plants, 2019, 5, 944-951.	4.7	141
67	Improved estimates of forest cover and loss in the Brazilian Amazon in 2000–2017. Nature Sustainability, 2019, 2, 764-772.	11.5	71
68	Assimilating Soil Moisture Retrieved from Sentinel-1 and Sentinel-2 Data into WOFOST Model to Improve Winter Wheat Yield Estimation. Remote Sensing, 2019, 11, 1618.	1.8	73
69	Winter Wheat Green-up Date Variation and its Diverse Response on the Hydrothermal Conditions over the North China Plain, Using MODIS Time-Series Data. Remote Sensing, 2019, 11, 1593.	1.8	10
70	Trends and controls of terrestrial gross primary productivity of China during 2000–2016. Environmental Research Letters, 2019, 14, 084032.	2.2	66
71	Increasing Outbreak of Cyanobacterial Blooms in Large Lakes and Reservoirs under Pressures from Climate Change and Anthropogenic Interferences in the Middle–Lower Yangtze River Basin. Remote Sensing, 2019, 11, 1754.	1.8	24
72	Continuous monitoring of lake dynamics on the Mongolian Plateau using all available Landsat imagery and Google Earth Engine. Science of the Total Environment, 2019, 689, 366-380.	3.9	116

#	Article	IF	CITATIONS
73	TROPOMI reveals dry-season increase of solar-induced chlorophyll fluorescence in the Amazon forest. Proceedings of the National Academy of Sciences of the United States of America, 2019, 116, 22393-22398.	3.3	78
74	Long-Term Dynamic of Poyang Lake Surface Water: A Mapping Work Based on the Google Earth Engine Cloud Platform. Remote Sensing, 2019, 11, 313.	1.8	71
75	Are There Sufficient Landsat Observations for Retrospective and Continuous Monitoring of Land Cover Changes in China?. Remote Sensing, 2019, 11, 1808.	1.8	20
76	Divergent shifts in peak photosynthesis timing of temperate and alpine grasslands in China. Remote Sensing of Environment, 2019, 233, 111395.	4.6	85
77	Assessing spatial-temporal dynamics of urban expansion, vegetation greenness and photosynthesis in megacity Shanghai, China during 2000–2016. Remote Sensing of Environment, 2019, 233, 111374.	4.6	100
78	Changes in area and number of nature reserves in China. Conservation Biology, 2019, 33, 1066-1075.	2.4	68
79	Estimating leaf area index and aboveground biomass of grazing pastures using Sentinel-1, Sentinel-2 and Landsat images. ISPRS Journal of Photogrammetry and Remote Sensing, 2019, 154, 189-201.	4.9	184
80	Rapid expansion of coastal aquaculture ponds in China from Landsat observations during 1984–2016. International Journal of Applied Earth Observation and Geoinformation, 2019, 82, 101902.	1.4	92
81	Assessing consistency of spring phenology of snow-covered forests as estimated by vegetation indices, gross primary production, and solar-induced chlorophyll fluorescence. Agricultural and Forest Meteorology, 2019, 275, 305-316.	1.9	64
82	Ecological engineering projects increased vegetation cover, production, and biomass in semiarid and subhumid Northern China. Land Degradation and Development, 2019, 30, 1620-1631.	1.8	71
83	Accelerating Cities in an Unsustainable Landscape: Urban Expansion and Cropland Occupation in China, 1990–2030. Sustainability, 2019, 11, 2283.	1.6	24
84	A Methodology for Flash Drought Identification: Application of Flash Drought Frequency across the United States. Journal of Hydrometeorology, 2019, 20, 833-846.	0.7	120
85	Does direct-seeded rice decrease ecosystem-scale methane emissions?—A case study from a rice paddy in southeast China. Agricultural and Forest Meteorology, 2019, 272-273, 118-127.	1.9	24
86	High resolution paddy rice maps in cloud-prone Bangladesh and Northeast India using Sentinel-1 data. Scientific Data, 2019, 6, 26.	2.4	107
87	Effects of reclamation and natural changes on coastal wetlands bordering China's Yellow Sea from 1984 to 2015. Land Degradation and Development, 2019, 30, 1533-1544.	1.8	38
88	Spatial, temporal, and spectral variations in albedo due to vegetation changes in China's grasslands. ISPRS Journal of Photogrammetry and Remote Sensing, 2019, 152, 1-12.	4.9	37
89	Analysis of Parameters for the Accurate and Fast Estimation of Tree Diameter at Breast Height Based on Simulated Point Cloud. Remote Sensing, 2019, 11, 2707.	1.8	3
90	Tracking Reforestation in the Loess Plateau, China after the "Grain for Green―Project through Integrating PALSAR and Landsat Imagery. Remote Sensing, 2019, 11, 2685.	1.8	14

#	Article	IF	CITATIONS
91	The relationships between urban-rural temperature difference and vegetation in eight cities of the Great Plains. Frontiers of Earth Science, 2019, 13, 290-302.	0.9	11
92	Evapotranspiration-dominated biogeophysical warming effect of urbanization in the Beijing-Tianjin-Hebei region, China. Climate Dynamics, 2019, 52, 1231-1245.	1.7	36
93	Global patterns of extreme drought-induced loss in land primary production: Identifying ecological extremes from rain-use efficiency. Science of the Total Environment, 2018, 628-629, 611-620.	3.9	69
94	Expansion dynamics of deciduous rubber plantations in Xishuangbanna, China during 2000–2010. GIScience and Remote Sensing, 2018, 55, 905-925.	2.4	30
95	Spatioâ€Temporal Convergence of Maximum Daily Lightâ€Use Efficiency Based on Radiation Absorption by Canopy Chlorophyll. Geophysical Research Letters, 2018, 45, 3508-3519.	1.5	48
96	Responses of gross primary production of grasslands and croplands under drought, pluvial, and irrigation conditions during 2010–2016, Oklahoma, USA. Agricultural Water Management, 2018, 204, 47-59.	2.4	38
97	Assessing the Extent and Impact of Online Data Sharing in Eddy Covariance Flux Research. Journal of Geophysical Research G: Biogeosciences, 2018, 123, 129-137.	1.3	21
98	Increased vegetation growth and carbon stock in China karst via ecological engineering. Nature Sustainability, 2018, 1, 44-50.	11.5	460
99	Divergent trends of open-surface water body area in the contiguous United States from 1984 to 2016. Proceedings of the National Academy of Sciences of the United States of America, 2018, 115, 3810-3815.	3.3	199
100	Multi-scale temporal variation of methane flux and its controls in a subtropical tidal salt marsh in eastern China. Biogeochemistry, 2018, 137, 163-179.	1.7	36
101	Mapping Forest and Their Spatial–Temporal Changes From 2007 to 2015 in Tropical Hainan Island by Integrating ALOS/ALOS-2 L-Band SAR and Landsat Optical Images. IEEE Journal of Selected Topics in Applied Earth Observations and Remote Sensing, 2018, 11, 852-867.	2.3	35
102	Characterizing the encroachment of juniper forests into sub-humid and semi-arid prairies from 1984 to 2010 using PALSAR and Landsat data. Remote Sensing of Environment, 2018, 205, 166-179.	4.6	61
103	On the relationship between sub-daily instantaneous and daily total gross primary production: Implications for interpreting satellite-based SIF retrievals. Remote Sensing of Environment, 2018, 205, 276-289.	4.6	91
104	Exacerbated grassland degradation and desertification in Central Asia during 2000–2014. Ecological Applications, 2018, 28, 442-456.	1.8	83
105	Underestimates of Grassland Gross Primary Production in MODIS Standard Products. Remote Sensing, 2018, 10, 1771.	1.8	36
106	Integrated Analyses of PALSAR and Landsat Imagery Reveal More Agroforests in a Typical Agricultural Production Region, North China Plain. Remote Sensing, 2018, 10, 1323.	1.8	10
107	Response of Tropical Terrestrial Gross Primary Production to the Super El Niño Event in 2015. Journal of Geophysical Research G: Biogeosciences, 2018, 123, 3193-3203.	1.3	24
108	The impact of surveillance and control on highly pathogenic avian influenza outbreaks in poultry in Dhaka division, Bangladesh. PLoS Computational Biology, 2018, 14, e1006439.	1.5	17

#	Article	IF	CITATIONS
109	Spatiotemporal Consistency of Four Gross Primary Production Products and Solarâ€Induced Chlorophyll Fluorescence in Response to Climate Extremes Across CONUS in 2012. Journal of Geophysical Research G: Biogeosciences, 2018, 123, 3140-3161.	1.3	30
110	Spatial analysis of dengue fever and exploration of its environmental and socio-economic risk factors using ordinary least squares: A case study in five districts of Guangzhou City, China, 2014. International Journal of Infectious Diseases, 2018, 75, 39-48.	1.5	47
111	Quantifying spatial-temporal changes of tea plantations in complex landscapes through integrative analyses of optical and microwave imagery. International Journal of Applied Earth Observation and Geoinformation, 2018, 73, 697-711.	1.4	13
112	Enhanced gross primary production and evapotranspiration in juniperâ€encroached grasslands. Global Change Biology, 2018, 24, 5655-5667.	4.2	25
113	Spatial-temporal consistency between gross primary productivity and solar-induced chlorophyll fluorescence of vegetation in China during 2007–2014. Science of the Total Environment, 2018, 639, 1241-1253.	3.9	36
114	Comparison of Pixel- and Object-Based Approaches in Phenology-Based Rubber Plantation Mapping in Fragmented Landscapes. Remote Sensing, 2018, 10, 44.	1.8	26
115	Carbon dioxide and water vapor fluxes in winter wheat and tallgrass prairie in central Oklahoma. Science of the Total Environment, 2018, 644, 1511-1524.	3.9	29
116	FluoSpec 2—An Automated Field Spectroscopy System to Monitor Canopy Solar-Induced Fluorescence. Sensors, 2018, 18, 2063.	2.1	67
117	Identifying Establishment Year and Pre-Conversion Land Cover of Rubber Plantations on Hainan Island, China Using Landsat Data during 1987–2015. Remote Sensing, 2018, 10, 1240.	1.8	25
118	Satelliteâ€Observed Major Greening and Biomass Increase in South China Karst During Recent Decade. Earth's Future, 2018, 6, 1017-1028.	2.4	143
119	Modeling gross primary production of paddy rice cropland through analyses of data from CO2 eddy flux tower sites and MODIS images. Remote Sensing of Environment, 2017, 190, 42-55.	4.6	42
120	Quantifying annual changes in built-up area in complex urban-rural landscapes from analyses of PALSAR and Landsat images. ISPRS Journal of Photogrammetry and Remote Sensing, 2017, 124, 89-105.	4.9	42
121	Status of land use intensity in China and its impacts on land carrying capacity. Journal of Chinese Geography, 2017, 27, 387-402.	1.5	44
122	Estimating aboveground biomass of broadleaf, needleleaf, and mixed forests in Northeastern China through analysis of 25-m ALOS/PALSAR mosaic data. Forest Ecology and Management, 2017, 389, 199-210.	1.4	29
123	Mapping the dynamics of eastern redcedar encroachment into grasslands during 1984–2010 through PALSAR and time series Landsat images. Remote Sensing of Environment, 2017, 190, 233-246.	4.6	65
124	Examining the short-term impacts of diverse management practices on plant phenology and carbon fluxes of Old World bluestems pasture. Agricultural and Forest Meteorology, 2017, 237-238, 60-70.	1.9	41
125	Modelling H5N1 in Bangladesh across spatial scales: Model complexity and zoonotic transmission risk. Epidemics, 2017, 20, 37-55.	1.5	19
126	Dominant role of plant physiology in trend and variability of gross primary productivity in North America. Scientific Reports, 2017, 7, 41366.	1.6	43

#	Article	IF	CITATIONS
127	Application of the space-for-time substitution method in validating long-term biomass predictions of a forest landscape model. Environmental Modelling and Software, 2017, 94, 127-139.	1.9	18
128	Continued decrease of open surface water body area in Oklahoma during 1984–2015. Science of the Total Environment, 2017, 595, 451-460.	3.9	118
129	Quantifying agricultural drought in tallgrass prairie region in the U.S. Southern Great Plains through analysis of a water-related vegetation index from MODIS images. Agricultural and Forest Meteorology, 2017, 246, 111-122.	1.9	40
130	Combining Spectral and Morphometric Properties of Landslides for Separating Individual Landslides Based on Object-Oriented Method. , 2017, , 61-70.		4
131	A global moderate resolution dataset of gross primary production of vegetation for 2000–2016. Scientific Data, 2017, 4, 170165.	2.4	335
132	Temporal consistency between gross primary production and solar-induced chlorophyll fluorescence in the ten most populous megacity areas over years. Scientific Reports, 2017, 7, 14963.	1.6	30
133	Annual dynamics of forest areas in South America during 2007–2010 at 50-m spatial resolution. Remote Sensing of Environment, 2017, 201, 73-87.	4.6	47
134	Longâ€ŧerm analysis of the asynchronicity between temperature and precipitation maxima in the United States Great Plains. International Journal of Climatology, 2017, 37, 3919-3933.	1.5	13
135	A mangrove forest map of China in 2015: Analysis of time series Landsat 7/8 and Sentinel-1A imagery in Google Earth Engine cloud computing platform. ISPRS Journal of Photogrammetry and Remote Sensing, 2017, 131, 104-120.	4.9	288
136	Assessing agricultural drought in summer over Oklahoma Mesonet sites using the water-related vegetation index from MODIS. International Journal of Biometeorology, 2017, 61, 377-390.	1.3	18
137	Analysis and estimation of tallgrass prairie evapotranspiration in the central United States. Agricultural and Forest Meteorology, 2017, 232, 35-47.	1.9	27
138	Spatiotemporal patterns of paddy rice croplands in China and India from 2000 to 2015. Science of the Total Environment, 2017, 579, 82-92.	3.9	127
139	Could Changes in the Agricultural Landscape of Northeastern China Have Influenced the Long-Distance Transmission of Highly Pathogenic Avian Influenza H5Nx Viruses?. Frontiers in Veterinary Science, 2017, 4, 225.	0.9	14
140	Different Patterns in Daytime and Nighttime Thermal Effects of Urbanization in Beijing-Tianjin-Hebei Urban Agglomeration. Remote Sensing, 2017, 9, 121.	1.8	31
141	Open Surface Water Mapping Algorithms: A Comparison of Water-Related Spectral Indices and Sensors. Water (Switzerland), 2017, 9, 256.	1.2	147
142	Intensifying poultry production systems and the emergence of avian influenza in China: a â€~One Health/Ecohealth' epitome. Archives of Public Health, 2017, 75, 48.	1.0	44
143	Mapping Annual Forest Cover in Sub-Humid and Semi-Arid Regions through Analysis of Landsat and PALSAR Imagery. Remote Sensing, 2016, 8, 933.	1.8	21
144	Global mapping of highly pathogenic avian influenza H5N1 and H5Nx clade 2.3.4.4 viruses with spatial cross-validation. ELife, 2016, 5, .	2.8	45

#	Article	IF	CITATIONS
145	Impact of Climate Change on Vegetation Growth in Arid Northwest of China from 1982 to 2011. Remote Sensing, 2016, 8, 364.	1.8	33
146	Variation in Cropping Intensity in Northern China from 1982 to 2012 Based on GIMMS-NDVI Data. Sustainability, 2016, 8, 1123.	1.6	27
147	Chewing Lice of Swan Geese (Anser cygnoides): New Host-Parasite Associations. Korean Journal of Parasitology, 2016, 54, 685-691.	0.5	0
148	Variability and Changes in Climate, Phenology, and Gross Primary Production of an Alpine Wetland Ecosystem. Remote Sensing, 2016, 8, 391.	1.8	51
149	Canopy and physiological controls of GPP during drought and heat wave. Geophysical Research Letters, 2016, 43, 3325-3333.	1.5	75
150	Spatial Modeling of Wild Bird Risk Factors for Highly Pathogenic A(H5N1) Avian Influenza Virus Transmission. Avian Diseases, 2016, 60, 329-336.	0.4	15
151	Comparison of solarâ€induced chlorophyll fluorescence, lightâ€use efficiency, and processâ€based <scp>GPP</scp> models in maize. Ecological Applications, 2016, 26, 1211-1222.	1.8	82
152	Precipitation and carbon-water coupling jointly control the interannual variability of global land gross primary production. Scientific Reports, 2016, 6, 39748.	1.6	57
153	Mapping tropical forests and deciduous rubber plantations in Hainan Island, China by integrating PALSAR 25-m and multi-temporal Landsat images. International Journal of Applied Earth Observation and Geoinformation, 2016, 50, 117-130.	1.4	69
154	Semi-natural areas of Tarim Basin in northwest China: Linkage to desertification. Science of the Total Environment, 2016, 573, 178-188.	3.9	22
155	Consistency between sun-induced chlorophyll fluorescence and gross primary production of vegetation in North America. Remote Sensing of Environment, 2016, 183, 154-169.	4.6	180
156	Canopy and climate controls of gross primary production of Mediterranean-type deciduous and evergreen oak savannas. Agricultural and Forest Meteorology, 2016, 226-227, 132-147.	1.9	19
157	Land claim and loss of tidal flats in the Yangtze Estuary. Scientific Reports, 2016, 6, 24018.	1.6	62
158	Explaining inter-annual variability of gross primary productivity from plant phenology and physiology. Agricultural and Forest Meteorology, 2016, 226-227, 246-256.	1.9	81
159	Mapping forests in monsoon Asia with ALOS PALSAR 50-m mosaic images and MODIS imagery in 2010. Scientific Reports, 2016, 6, 20880.	1.6	49
160	Mapping paddy rice planting area in rice-wetland coexistent areas through analysis of Landsat 8 OLI and MODIS images. International Journal of Applied Earth Observation and Geoinformation, 2016, 46, 1-12.	1.4	103
161	Multiple afforestation programs accelerate the greenness in the †Three North' region of China from 1982 to 2013. Ecological Indicators, 2016, 61, 404-412.	2.6	264
162	Mapping rice cropping systems using Landsat-derived Renormalized Index of Normalized Difference Vegetation Index (RNDVI) in the Poyang Lake Region, China. Frontiers of Earth Science, 2016, 10, 303-314.	0.9	16

#	Article	IF	CITATIONS
163	Mapping paddy rice planting area in northeastern Asia with Landsat 8 images, phenology-based algorithm and Google Earth Engine. Remote Sensing of Environment, 2016, 185, 142-154.	4.6	524
164	Mapping paddy rice distribution using multi-temporal Landsat imagery in the Sanjiang Plain, northeast China. Frontiers of Earth Science, 2016, 10, 49-62.	0.9	39
165	A new method for discovering behavior patterns among animal movements. International Journal of Geographical Information Science, 2016, 30, 929-947.	2.2	8
166	Movement analysis of free-grazing domestic ducks in Poyang Lake, China: a disease connection. International Journal of Geographical Information Science, 2016, 30, 869-880.	2.2	19
167	Effects of in-situ and reanalysis climate data on estimation of cropland gross primary production using the Vegetation Photosynthesis Model. Agricultural and Forest Meteorology, 2015, 213, 240-250.	1.9	29
168	Mapping paddy rice planting area in wheat-rice double-cropped areas through integration of Landsat-8 OLI, MODIS and PALSAR images. Scientific Reports, 2015, 5, 10088.	1.6	55
169	Stable Isotopes Suggest Low Site Fidelity in Bar-Headed Geese (<i>Anser indicus</i>) in Mongolia: Implications for Disease Transmission. Waterbirds, 2015, 38, 123-220.	0.2	5
170	Mapping Deciduous Rubber Plantation Areas and Stand Ages with PALSAR and Landsat Images. Remote Sensing, 2015, 7, 1048-1073.	1.8	89
171	Mapping Oil Palm Plantations in Cameroon Using PALSAR 50-m Orthorectified Mosaic Images. Remote Sensing, 2015, 7, 1206-1224.	1.8	52
172	Estimation and analysis of gross primary production of soybean under various management practices and drought conditions. ISPRS Journal of Photogrammetry and Remote Sensing, 2015, 99, 70-83.	4.9	62
173	Tracking the dynamics of paddy rice planting area in 1986–2010 through time series Landsat images and phenology-based algorithms. Remote Sensing of Environment, 2015, 160, 99-113.	4.6	257
174	Modeling gross primary production of maize and soybean croplands using light quality, temperature, water stress, and phenology. Agricultural and Forest Meteorology, 2015, 213, 160-172.	1.9	26
175	Mapping paddy rice planting areas through time series analysis of MODIS land surface temperature and vegetation index data. ISPRS Journal of Photogrammetry and Remote Sensing, 2015, 106, 157-171.	4.9	207
176	Influencing factors of households disadvantaged in post-earthquake life recovery: a case study of the Wenchuan earthquake in China. Natural Hazards, 2015, 75, 1853-1869.	1.6	29
177	Spatial characterization of colonies of the flying fox bat, a carrier of Nipah Virus in Thailand. BMC Veterinary Research, 2015, 11, 81.	0.7	20
178	Mapping migratory flyways in Asia using dynamic Brownian bridge movement models. Movement Ecology, 2015, 3, 3.	1.3	65
179	Comparison of four EVI-based models for estimating gross primary production of maize and soybean croplands and tallgrass prairie under severe drought. Remote Sensing of Environment, 2015, 162, 154-168.	4.6	93
180	Mapping paddy rice planting area in cold temperate climate region through analysis of time series Landsat 8 (OLI), Landsat 7 (ETM+) and MODIS imagery. ISPRS Journal of Photogrammetry and Remote Sensing, 2015, 105, 220-233.	4.9	118

#	Article	IF	CITATIONS
181	Sensitivity analysis of vegetation indices to drought over two tallgrass prairie sites. ISPRS Journal of Photogrammetry and Remote Sensing, 2015, 108, 151-160.	4.9	68
182	Forest cover maps of China in 2010 from multiple approaches and data sources: PALSAR, Landsat, MODIS, FRA, and NFI. ISPRS Journal of Photogrammetry and Remote Sensing, 2015, 109, 1-16.	4.9	70
183	Biophysical controls on carbon and water vapor fluxes across a grassland climatic gradient in the United States. Agricultural and Forest Meteorology, 2015, 214-215, 293-305.	1.9	51
184	Mapping Earthquake Risk of the World. IHDP/Future Earth-integrated Risk Governance Project Series, 2015, , 25-39.	0.2	9
185	A 50-m Forest Cover Map in Southeast Asia from ALOS/PALSAR and Its Application on Forest Fragmentation Assessment. PLoS ONE, 2014, 9, e85801.	1.1	46
186	Mapping Forest Biomass Using Remote Sensing and National Forest Inventory in China. Forests, 2014, 5, 1267-1283.	0.9	74
187	Comparison of Gross Primary Productivity Derived from GIMMS NDVI3g, GIMMS, and MODIS in Southeast Asia. Remote Sensing, 2014, 6, 2108-2133.	1.8	59
188	Predicting the risk of avian influenza A H7N9 infection in live-poultry markets across Asia. Nature Communications, 2014, 5, 4116.	5.8	145
189	Modeling Carbon Fluxes Using Multi-Temporal MODIS Imagery and CO2 Eddy Flux Tower Data in Zoige Alpine Wetland, South-West China. Wetlands, 2014, 34, 603-618.	0.7	30
190	Multiple cropping intensity in China derived from agro-meteorological observations and MODIS data. Chinese Geographical Science, 2014, 24, 205-219.	1.2	60
191	The time process of postâ€earthquake recovery: the Yao'an earthquake in China. Disasters, 2014, 38, 774-789.	1.1	9
192	Sensitivity of vegetation indices and gross primary production of tallgrass prairie to severe drought. Remote Sensing of Environment, 2014, 152, 1-14.	4.6	103
193	Bird migration and avian influenza: A comparison of hydrogen stable isotopes and satellite tracking methods. Ecological Indicators, 2014, 45, 266-273.	2.6	25
194	Largeâ€scale estimation and uncertainty analysis of gross primary production in Tibetan alpine grasslands. Journal of Geophysical Research G: Biogeosciences, 2014, 119, 466-486.	1.3	50
195	Impacts of ecological restoration projects on agricultural productivity in China. Journal of Chinese Geography, 2013, 23, 404-416.	1.5	33
196	Climate change affecting temperature and aridity zones: a case study in Eastern Inner Mongolia, China from 1960–2008. Theoretical and Applied Climatology, 2013, 113, 561-572.	1.3	18
197	Phenology and gross primary production of two dominant savanna woodland ecosystems in Southern Africa. Remote Sensing of Environment, 2013, 135, 189-201.	4.6	82
198	Mapping deciduous rubber plantations through integration of PALSAR and multi-temporal Landsat imagery. Remote Sensing of Environment, 2013, 134, 392-402.	4.6	183

#	Article	IF	CITATIONS
199	Green-up dates in the Tibetan Plateau have continuously advanced from 1982 to 2011. Proceedings of the United States of America, 2013, 110, 4309-4314.	3.3	528
200	Modelling gross primary production in semi-arid Inner Mongolia using MODIS imagery and eddy covariance data. International Journal of Remote Sensing, 2013, 34, 2829-2857.	1.3	26
201	A comparison of forest cover maps in Mainland Southeast Asia from multiple sources: PALSAR, MERIS, MODIS and FRA. Remote Sensing of Environment, 2012, 127, 60-73.	4.6	91
202	Changes in rice cropping systems in the Poyang Lake Region, China during 2004–2010. Journal of Chinese Geography, 2012, 22, 653-668.	1.5	52
203	Integrating SAR and optical imagery for regional mapping of paddy rice attributes in the Poyang Lake Watershed, China. Canadian Journal of Remote Sensing, 2011, 37, 17-26.	1.1	32
204	Quantifying the area and spatial distribution of double- and triple-cropping croplands in India with multi-temporal MODIS imagery in 2005. International Journal of Remote Sensing, 2011, 32, 367-386.	1.3	100
205	A library of georeferenced photos from the field. Eos, 2011, 92, 453-454.	0.1	36
206	Modeling gross primary production of irrigated and rain-fed maize using MODIS imagery and CO2 flux tower data. Agricultural and Forest Meteorology, 2011, 151, 1514-1528.	1.9	99
207	Victims and Vectors: Highly Pathogenic Avian Influenza H5N1 and the Ecology of Wild Birds. Avian Biology Research, 2010, 3, 51-73.	0.4	45
208	A Simple Algorithm for Large-Scale Mapping of Evergreen Forests in Tropical America, Africa and Asia. Remote Sensing, 2009, 1, 355-374.	1.8	54
209	Modeling gross primary productivity for winter wheat–maize double cropping system using MODIS time series and CO2 eddy flux tower data. Agriculture, Ecosystems and Environment, 2009, 129, 391-400.	2.5	106
210	Light absorption by leaf chlorophyll and maximum light use efficiency. IEEE Transactions on Geoscience and Remote Sensing, 2006, 44, 1933-1935.	2.7	39
211	Mapping paddy rice agriculture in South and Southeast Asia using multi-temporal MODIS images. Remote Sensing of Environment, 2006, 100, 95-113.	4.6	667
212	Detecting leaf phenology of seasonally moist tropical forests in South America with multi-temporal MODIS images. Remote Sensing of Environment, 2006, 103, 465-473.	4.6	179
213	Satellite-based modeling of gross primary production in a seasonally moist tropical evergreen forest. Remote Sensing of Environment, 2005, 94, 105-122.	4.6	242
214	Mapping paddy rice agriculture in southern China using multi-temporal MODIS images. Remote Sensing of Environment, 2005, 95, 480-492.	4.6	814
215	Spatial analysis of growing season length control over net ecosystem exchange. Global Change Biology, 2005, 11, 1777-1787.	4.2	313
216	MODELING GROSS PRIMARY PRODUCTION OF AN EVERGREEN NEEDLELEAF FOREST USING MODIS AND CLIMATE DATA. , 2005, 15, 954-969.		177

#	Article	IF	CITATIONS
217	Satellite-based modeling of gross primary production in an evergreen needleleaf forest. Remote Sensing of Environment, 2004, 89, 519-534.	4.6	682
218	Sensitivity of vegetation indices to atmospheric aerosols: continental-scale observations in Northern Asia. Remote Sensing of Environment, 2003, 84, 385-392.	4.6	153
219	Reduced methane emissions from large-scale changes in water management of China's rice paddies during 1980-2000. Geophysical Research Letters, 2002, 29, 33-1-33-4.	1.5	134
220	Combining remote sensing and ground census data to develop new maps of the distribution of rice agriculture in China. Global Biogeochemical Cycles, 2002, 16, 38-1-38-10.	1.9	267
221	Characterization of forest types in Northeastern China, using multi-temporal SPOT-4 VEGETATION sensor data. Remote Sensing of Environment, 2002, 82, 335-348.	4.6	277
222	Water-related land cover data products for geospatial analysis and modeling of infectious disease transmission risks. Frontiers in Veterinary Science, 0, 6, .	0.9	0